



Frequency Chirp Characterization of Silicon Ring Resonator Modulators

Erwan Weckenmann, Laurent Bramerie, Mathilde Gay, Diego Perez-Galacho, Frederic Boeuf, Lucas Deniel, Delphine Marris-Morini, Christophe Peucheret

► To cite this version:

Erwan Weckenmann, Laurent Bramerie, Mathilde Gay, Diego Perez-Galacho, Frederic Boeuf, et al.. Frequency Chirp Characterization of Silicon Ring Resonator Modulators. IEEE Photonics Technology Letters, 2022, 34 (12), pp.653-656. 10.1109/LPT.2022.3179650 . hal-03693026

HAL Id: hal-03693026

<https://hal.science/hal-03693026>

Submitted on 10 Jun 2022

HAL is a multi-disciplinary open access archive for the deposit and dissemination of scientific research documents, whether they are published or not. The documents may come from teaching and research institutions in France or abroad, or from public or private research centers.

L'archive ouverte pluridisciplinaire **HAL**, est destinée au dépôt et à la diffusion de documents scientifiques de niveau recherche, publiés ou non, émanant des établissements d'enseignement et de recherche français ou étrangers, des laboratoires publics ou privés.

Frequency Chirp Characterization of Silicon Ring Resonator Modulators

Erwan Weckenmann, Laurent Bramerie, Mathilde Gay, Diego Pérez-Galacho, Frédéric Boeuf, Lucas Deniel, Delphine Marris-Morini and Christophe Peucheret

Abstract—The frequency chirping properties of silicon ring resonator modulators (RRMs) are experimentally investigated under sinusoidal modulation. The modulated electric field at the output of an RRM is measured in the time domain thanks to a coherent detection system. The power and phase waveforms are then analyzed in terms of their temporal phase and amplitude for different wavelength detunings between the optical source and the resonance and for different modulation frequencies. The evolution of the frequency chirp, described through a peak-to-peak chirp parameter, is quantified as a function of wavelength detuning and modulation frequency for the first time.

Index Terms—Frequency chirp, intensity modulation, optical communications, phase modulation, ring resonator modulator, silicon photonics.

I. INTRODUCTION

SILICON ring resonator modulators are promising devices for short-distance optical communication systems thanks to their compactness, energy efficiency and low cost. Their resonant nature enables highly-efficient intensity modulation (IM) [1]. Short-distance systems based on direct-detection, such as the inter data center links that are the objects of significant interest at the present time, can reach transmission lengths exceeding 80 km over standard single-mode fibers that are dispersive at $1.5 \mu\text{m}$ [2]. The frequency chirp properties of RRM are therefore of high importance for such applications, since the chirp can interact with dispersion and reduce the transmission length. However, frequency chirping in RRM has been the object of only very few studies so far. The chirp parameter of silicon RRM has been evaluated thanks to numerical models based on the applied voltage-induced variations of the transmission and phase of micro-resonator transfer functions calculated using either the temporal coupled-mode theory [3] or a scattering matrix approach [4]. The dependence of the chirp on the modulation frequency and on the laser-resonance detuning has however not been fully assessed. Some preliminary experimental characterizations based on measurements of the instantaneous variations of the frequency using an interferometer have been presented in [5].

E. Weckenmann, L. Bramerie, M. Gay and C. Peucheret are with Univ Rennes, CNRS, FOTON – UMR 6082, F-22305 Lannion, France (e-mail: erwan.weckenmann@univ-rennes1.fr).

D. Pérez-Galacho was with Université Paris-Saclay, CNRS, Centre de Nanosciences et de Nanotechnologies, 91120 Palaiseau, France. He is now at ITEAM Research Institute, Universitat Politècnica de València, Camino de Vera s/n, 46022 Valencia, Spain.

F. Boeuf is with ST Microelectronics, 850 rue Jean Monnet, 38920 Crolles, France.

L. Deniel and D. Marris-Morini are with Université Paris-Saclay, CNRS, Centre de Nanosciences et de Nanotechnologies, 91120 Palaiseau, France.

The impact of the frequency chirp could also be observed from measurements of the small-signal frequency responses of dispersive direct-detection channels [4], [5].

However, a comprehensive investigation of the frequency chirping properties of silicon RRM is, so far, still lacking. We have recently reported a preliminary frequency chirp characterization of a silicon RRM where the dependence of the frequency chirp on the wavelength detuning between the laser source and the resonance and on the modulation frequency has been highlighted [6]. In this work, we complement the results of [6] by providing a new analysis of the frequency chirping properties of silicon RRM by comparing the relative phases between the emitted power and instantaneous frequency waveforms as well as their amplitudes under sinusoidal modulation. Both waveforms are measured in the time domain thanks to a coherent detection system and are then compared to a numerical model, showing a good qualitative agreement. The chirp parameter is then calculated for different wavelength detunings and modulation frequencies.

II. RRM AND FREQUENCY CHIRP CHARACTERIZATION

The considered RRM makes use of a standard all-pass configuration with a carrier-depletion based phase-shifter implemented as a lateral PN junction in the ring waveguide. It is known that an over-coupled RRM can give rise to an effective negative α chirp parameter, which is beneficial for transmission over positive (D parameter) dispersion fiber [3]. Our study is therefore restricted to an over-coupled RRM. The modulation depth depends on the total Q -factor of the resonance, which is determined by the self-coupling coefficient σ of the directional coupler and the round-trip field loss a in the ring waveguide. The electric field E_{out} at the output of the all-pass port of the RRM can be obtained from the input electric field E_{in} according to

$$\frac{E_{\text{out}}}{E_{\text{in}}} = \frac{\sigma - ae^{-j\phi_r}}{1 - \sigma ae^{-j\phi_r}} \quad (1)$$

where ϕ_r is the phase shift accumulated over the ring waveguide length. In what follows, the dynamics of the RRM is simulated according to the model proposed in [7], in order to estimate the frequency chirp of the studied RRM. The plasma dispersion effect is responsible for the desired modulation of ϕ_r as well as spurious modulation of the attenuation a [8]. Both effects are taken into account in the model.

The RRM used for the experimental characterization has a radius of $20 \mu\text{m}$ and a Q -factor of 3×10^4 in the absence of applied voltage. This RRM is fabricated from rib waveguides

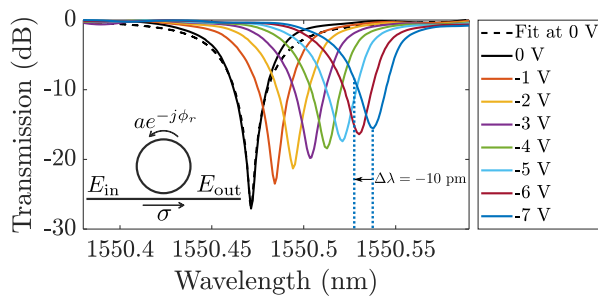


Fig. 1. Measured static transfer functions of the RRM for different applied DC voltages (solid lines). The dashed black line represents a fit of the static transfer function according to equation (1) for a DC voltage of 0 V. The wavelength detuning $\Delta\lambda = -10$ pm between source and resonance wavelengths at -7 V corresponds to where the maximum modulation depth is obtained.

of 400-nm width and 150-nm etching depth for a 310-nm total silicon height. The doping concentrations of the P doped and N doped regions are $5 \times 10^{17} \text{ cm}^{-3}$ and 10^{18} cm^{-3} , respectively [9]. Fig. 1 shows static transfer functions of the RRM measured using a tunable continuous wave (CW) laser source and a power meter when different direct current (DC) voltage values are applied to the phase shifter. The PN junction tolerates applied voltage values between 0 V and -14 V without generating current flows that could otherwise induce a significant thermal contribution to the induced phase shift and resulting detuning. The optical power of the CW source is limited to -5 dBm in order to avoid nonlinear effects in silicon that could make the intensity transfer function asymmetric on both sides of the resonance frequency [10]. The optical wave is injected at the input of the RRM and retrieved at the output vertically thanks to grating couplers. Coupling and loss parameters are then retrieved for this ring at each applied voltage by fitting the corresponding static transfer functions with equation (1), as shown in Fig. 1. The extracted values of σ and a are then used in the dynamical model.

In the following, we will characterize the frequency chirp of the RRM from the common definition of the chirp parameter

$$\alpha(t) = \frac{\frac{d\phi(t)}{dt}}{\frac{1}{2P(t)} \frac{dP(t)}{dt}}, \quad (2)$$

which describes the relation between the IM and the phase modulation (PM) at the output of an electro-optic modulator [11]. $\phi(t)$ and $P(t)$ represent the optical phase and power, respectively, at the output of the RRM. In order to fully characterize the frequency chirp of the RRM, the variations of the amplitude and the phase of the electric field of the modulated signal have to be measured for a given detuning between the wavelength of the CW laser source (λ_s) and that of the resonance (λ_0), at a given bias voltage. The wavelength detuning is defined according to $\Delta\lambda = \lambda_s - \lambda_0$. The frequency chirp also needs to be characterized as a function of modulation frequency. For this purpose, the coherent heterodyne setup represented in Fig. 2 is used. A radio frequency oscillator (RFO) generates a sinusoidal voltage with a peak-to-peak amplitude of 1 V at a chosen modulation frequency, which is applied to the phase-shifter of the RRM with a DC bias voltage of -7 V added using a bias tee. These voltage values are used for every set of parameters in the following characterization.

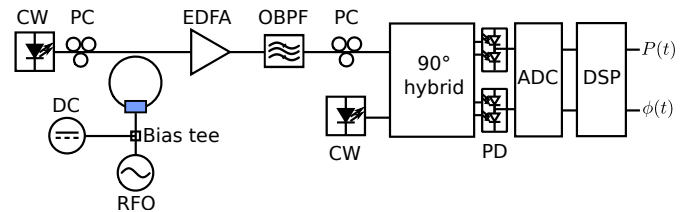


Fig. 2. Experimental setup. CW: continuous wave. PC: polarization controller. DC: direct current. RFO: radio frequency oscillator. EDFA: erbium-doped fiber amplifier. OBPF: optical bandpass filter. PD: photodiodes. ADC: analog-to-digital conversion. DSP: digital signal processing.

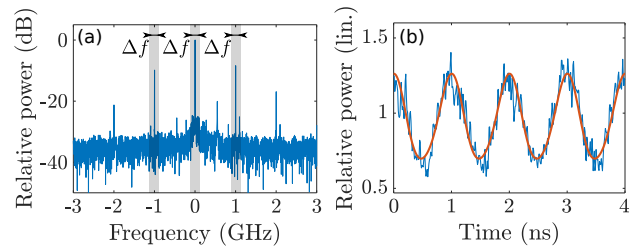


Fig. 3. (a) Power spectrum of the sampled recovered electric field corresponding to a signal modulated at 1 GHz for a detuning value of +20 pm. The grayed areas represent the filtered frequencies where $\Delta f = 10$ MHz is the filter bandwidth. (b) Recovered power waveforms before (blue line) and after (red line) filtering.

The modulated optical wave is amplified using an erbium-doped fiber amplifier (EDFA), then filtered using an optical band-pass filter (OBPF) to suppress out-of-band spontaneous emission noise, and finally input to a coherent front-end together with a CW signal generated by a local oscillator (LO) laser. A polarization controller (PC) is used to align the polarization state of the CW source with the polarization mode of the RRM waveguides, and another PC is used to align the polarization state of the modulated wave with that of the LO. The coherent receiver front-end is made of a 90-degree hybrid and balanced photodiodes with 25-GHz bandwidth. The linewidths of the signal and LO CW lasers are both equal to 100 kHz. The carrier frequency offset (CFO) between the LO and signal is kept below 300 MHz. The detected in-phase and quadrature components are then sampled at 100 GS/s in a real-time sampling oscilloscope with 33-GHz bandwidth. The real and imaginary parts of the modulated electric field envelope can then be recovered after digital CFO compensation. In order to remove out-of-band noise, which would result in noisy amplitude and phase waveforms, in turn resulting in unreliable estimates of the derivatives in equation (2), the carrier and first-order modulation sidebands of the recovered field envelope are digitally filtered with Gaussian bandpass filters with full-width at half-maximum bandwidth of 10 MHz, as shown in Fig. 3. Second-order harmonics can also be observed in Fig. 3(a) in the modulated signal power spectrum retrieved by the coherent receiver for a detuning of $\Delta\lambda = +20$ pm. Nevertheless, the measured power ratio between first-order and second-order sidebands is sufficiently large (i.e. 8 dB at $\Delta\lambda = +20$ pm and more for other detunings) so that the effect of harmonics on the measured waveforms can be neglected.

III. RESULTS AND DISCUSSION

The frequency modulation (FM) waveform defined as $\Delta\nu(t) = \frac{1}{2\pi} \frac{d\phi(t)}{dt}$ is compared to the power waveform in

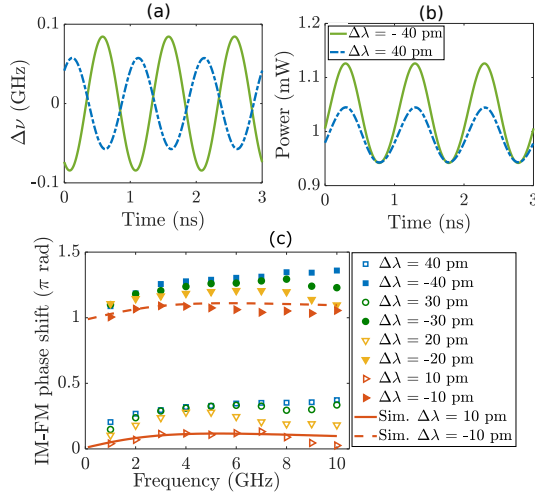


Fig. 4. Measured (a) instantaneous frequency and (b) power waveforms for detunings of -40 pm and $+40$ pm at a modulation frequency of 1 GHz. (c) Measured and simulated IM-FM phase shift as a function of the modulation frequency for different detunings.

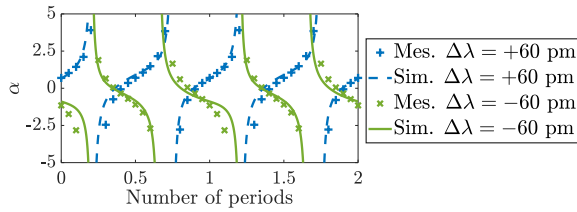


Fig. 5. Chirp parameter as a function of the number of time periods of the modulation signal for detunings of -60 pm and $+60$ pm at a modulation frequency of 5 GHz. The markers represent the chirp parameter retrieved from the measured samples. The solid lines represent the simulated chirp parameter.

order to understand the chirp behavior. Fig. 4(a) and (b) show the measured frequency and power waveforms at a modulation frequency of 1 GHz for detunings of $\Delta\lambda = \pm 40$ pm. In order to compare the IM-FM time phase shift for opposite detunings, the power waveforms are manually put in phase, as shown in Fig. 4(b), which enables a comparison of the FM waveforms in Fig. 4(a). Firstly, a π difference is observed between IM-FM phase shifts measured for opposite detunings, which results in opposite waveforms, directly impacting the sign of the chirp parameter. The same behavior can be observed for other modulation frequencies and detunings, as shown in Fig. 4(c). A simple analysis under small-signal sinusoidal modulation of the chirp parameter defined according to equation (2) shows that, unless the phase shift between IM and FM is equal to $\frac{\pi}{2}$, $\alpha(t)$ diverges with a period of $1/2f_m$, where f_m is the modulation frequency. The IM-FM phase shift being different from $\frac{\pi}{2}$ according to Fig. 4(c), such a divergent behavior is expected. Indeed, Fig. 5 confirms that the α parameter, represented here for detunings of ± 60 pm at a modulation frequency of 5 GHz, presents two divergent branches per period of the modulating signal.

In order to circumvent difficulties associated with the divergent nature of the instantaneous chirp parameter $\alpha(t)$, a new chirp metric that is based on the amplitudes of the variations of the phase and power waveforms, independently of their relative phase, is introduced [3], [12]. The peak-to-peak chirp

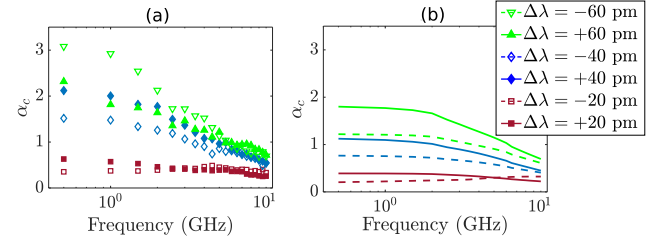


Fig. 6. (a) Measured and (b) simulated α_c parameter as a function of the modulation frequency for detunings of ± 20 pm, ± 40 pm, and ± 60 pm.

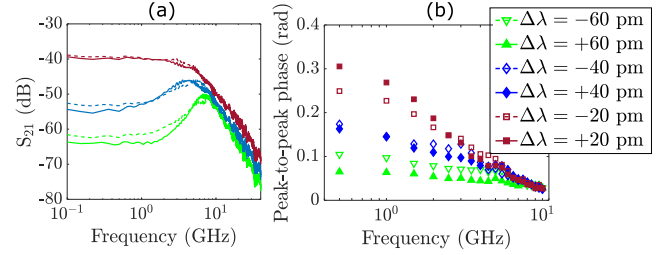


Fig. 7. (a) S_{21} frequency response measurements for different detunings. (b) Measured peak-to-peak phase as a function of modulation frequency for different detunings.

parameter α_c is defined as

$$\alpha_c = 2 \frac{\max[\phi(t)] - \min[\phi(t)]}{\ln(\max[P(t)]) - \ln(\min[P(t)])}. \quad (3)$$

Fig. 6(a) and (b) show the measured and calculated peak-to-peak chirp parameter, respectively, as a function of modulation frequency for detunings of $\Delta\lambda = \pm 20$ pm, ± 40 pm and ± 60 pm. The α_c parameter shows different values for opposite detunings. This is mainly due to different modulation efficiencies, as seen on the different sinusoid amplitudes, for opposite detunings in Fig. 4(b). This is caused by the loss modulation of the cavity, leading to an asymmetric modulation depth with respect to the resonance wavelength [13]. Furthermore, it can be seen from both measurements and simulations that the α_c parameter has higher variations with the detuning value at low frequencies. Then, for a given detuning, α_c remains rather constant at low frequencies and starts to decrease at high modulation frequencies.

In order to understand these tendencies, the peak-to-peak power and phase can be analyzed separately. Fig. 7(a) represents S_{21} measurements obtained from a vector network analyzer for different detunings. At low frequencies, the S_{21} parameter, or equivalently the peak-to-peak power representing the denominator of equation (3), decreases as the absolute value of the detuning increases, which is expected as the larger the detuning the smaller the modulation depth. Moreover, for a given detuning, the S_{21} parameter remains rather constant until a resonance effect is observed when the modulation frequency is equal to the detuning. This effect, due to asymmetric sideband generation, was also observed and described in [14] and corresponds to the case where one modulation sideband is almost suppressed since it matches the resonance frequency. At high frequencies, all S_{21} parameters decrease because of the electro-optic bandwidth limitation of the modulator. Besides, the peak-to-peak phase retrieved from the electric field measurements in the time domain, representing the numerator

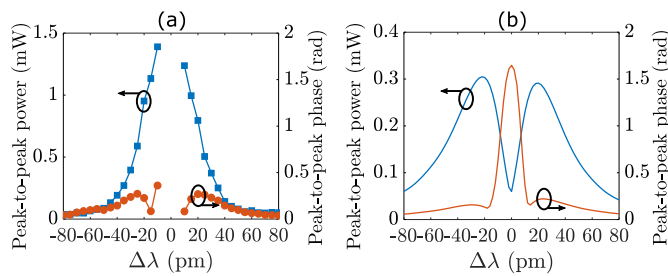


Fig. 8. (a) Measured and (b) simulated peak-to-peak power (IM amplitude) and peak-to-peak phase (PM amplitude) as a function of detuning for a modulation frequency of 1 GHz.

of equation (3) is shown in Fig. 7(b) and decreases with the modulation frequency. This behavior emphasizes even more the decrease tendency of the α_c parameter with the modulation frequency.

Fig. 8(a) and (b) show the measured and simulated peak-to-peak power and peak-to-peak phase as a function of detuning for a modulation frequency of 1 GHz. The range of detuning between $\Delta\lambda = -5$ pm and $\Delta\lambda = +5$ pm is excluded from the experimental characterization since the modulation is no longer linear, nor efficient, over this range due to the proximity between the resonance wavelength and the source wavelength. The measured peak-to-peak power shows high variations compared to the measured peak-to-peak phase for absolute values of the detuning between 20 pm and 40 pm, which confirms the predominant impact of the peak-to-peak power on the α_c parameter in this range of detunings. Fig. 8 also shows that the quantitative differences of the chirp between measurements and simulation at low frequencies essentially come from the peak-to-peak power contribution. The difference can be due to several approximations in the model such as the electrical properties and the carrier dynamics that are not considered, which could impact the modulation depth and therefore the RRM's bandwidth. Also, the coupling losses are not known and are considered as negligible.

The full dependence of α_c on wavelength detuning and modulation frequency is then measured and simulated, as shown in Fig. 9. It can be seen that the highest α_c values are obtained at low modulation frequencies (i.e. 1 GHz for this RRM) and at relatively high detunings (i.e. $\Delta\lambda = \pm 70$ pm for this RRM). The previous observations concerning the evolution of α_c as a function of the modulation frequency and the detuning independently are valid for any couple of these two parameters, in a modulation frequency range from 0.5 GHz to 10 GHz, and a wavelength detuning range from -80 pm to $+80$ pm.

IV. CONCLUSION

The frequency chirping properties of a silicon RRM have been experimentally and numerically characterized by studying the relative phases and peak-to-peak values of the modulated power and phase waveforms under sinusoidal modulation. The temporal phase relations between IM and FM show a π difference for opposite detunings and different values as a function of the wavelength detuning and the modulation frequency, leading to a divergent behavior of the commonly defined chirp

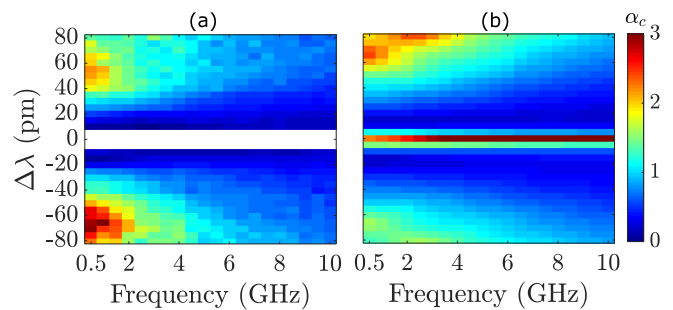


Fig. 9. α_c parameter retrieved from (a) measurements and (b) simulation.

parameter as a function of time. Thus, the frequency chirp was also quantified using a peak-to-peak chirp parameter metric. The strong dependence of the chirp parameter on the wavelength detuning and on the modulation frequency was analyzed from both measurements and simulation, from which a good qualitative agreement was obtained. This study shows that the chirp parameter has higher values at low frequencies and high detunings and is mostly influenced by the peak-to-peak power contribution. This comprehensive investigation provides, for the first time to our knowledge, a better understanding of the peculiar frequency chirping properties of silicon RRM, which can be used in order to optimize their utilization in high-speed communication applications.

REFERENCES

- [1] J. Witzens, "High-speed silicon photonics modulators," *Proc. IEEE*, vol. 106, no. 12, pp. 2158-2182, 2018.
- [2] J. Krause Perin, A. Shastri, and J. M. Kahn, "Data center links beyond 100 Gbit/s per wavelength," *Opt. Fiber Technol.*, vol. 44, pp. 69-85, 2018.
- [3] Z. Wang, Y. Gao, A. S. Kashi, J. C. Cartledge, and A. P. Knights, "Silicon microring modulator for dispersion uncompensated transmission applications," *J. Lightw. Technol.*, vol. 34, no. 16, pp. 3675-3681, 2016.
- [4] O. Dubray and S. Menezes, "Simulation and measurements of chirp penalties for silicon ring resonator modulators," *IEEE Photon. Technol. Lett.*, vol. 28, no. 3, pp. 280-283, 2016.
- [5] M. E. Chaibi, O. Dubray, L. Bramerie, K. Hassan, and C. Peucheret, "Multiple-band OFDM transmission exploiting the frequency chirping properties of silicon ring-resonator modulators," in *Asia Communications and Photonics Conference*, (Optical Society of America, 2017), M2G.1.
- [6] E. Weckenmann, L. Bramerie, M. Gay, D. Pérez-Galacho, F. Boeuf, L. Deniel, D. Marris-Morini, and C. Peucheret, "Comprehensive frequency chirp characterization of silicon ring resonator modulators," in *OSA Advanced Photonics Congress 2020 (IPR)*, (Optical Society of America, 2020), ITu1A.4.
- [7] W. D. Sacher and J. K. S. Poon, "Dynamics of microring resonator modulators," *Opt. Express*, vol. 16, no. 20, pp. 15741-15753, 2008.
- [8] R. A. Soref and B. R. Bennett, "Electrooptical effects in silicon," *IEEE J. Quantum Electron.*, vol. QE-23, no. 1, pp. 123-129, 1987.
- [9] D. Marris-Morini, L. Viot, C. Baudot, J.-M. Fédéli, G. Rasigade, D. Pérez-Galacho, J.-M. Hartmann, S. Olivier, P. Brindel, P. Crozat, F. Boeuf, and L. Vivien, "A 40 Gbit/s optical link on a 300-mm silicon platform," *Opt. Express*, vol. 22, no. 6, pp. 6674-6679, 2014.
- [10] T. Uesugi, B.-S. Song, T. Asano and S. Noda, "Investigation of optical nonlinearities in an ultra-high-Q Si nanocavity in a two-dimensional photonic crystal slab," *Opt. Express*, vol. 14, no. 1, pp. 377-386, 2006.
- [11] F. Koyama and K. Oga, "Frequency chirping in external modulators," *J. Lightw. Technol.*, vol. 6, no. 1, pp. 87-93, 1988.
- [12] J. C. Cartledge, "Comparison of effective α -parameters for semiconductor Mach-Zehnder optical modulators," *J. Lightw. Technol.*, vol. 16, no. 3, pp. 372-379, 1998.
- [13] K. Lengle, T. N. Nguyen, M. Gay, L. Bramerie, J. C. Simon, A. Bazin, F. Raineri and R. Raj, "Modulation contrast optimization for wavelength conversion of a 20 Gbit/s data signal in hybrid InP/SOI photonic crystal nanocavity," *Opt. Lett.*, vol. 39, no. 8, pp. 2298-2301, 2014.
- [14] J. Müller, F. Merget, S. Sharif Azadeh, J. Hauck, S. Romero Garcia, B. Shen, and J. Witzens, "Optical peaking enhancement in high-speed ring modulators," *Sci. Rep.*, vol. 4, Art. no. 6310, 2014.